Towards an Improved Retrieval of Ice Cloud Properties

CM-SAF Visiting Scientist Activity

Steffen Meyer[1], Andreas Macke[1] and Rob Roebeling[2]

[1] IFM-GEOMAR, Kiel, Germany
[2] KNMI, De Bilt, The Netherlands

Kiel, March 2007

Chapter 1

Introduction

The retrieval of cloud properties for cirrus clouds is very sensitive to the selected cloud characteristics and surface reflection in the required radiative transfer calculations. For ice clouds the retrieval of optical depth and particle size is based on simple ice crystal distributions. Currently, the Ice Water Path (IWP) is calculated with the cloud Liquid Water Path (LWP) equation based on optical depth and particle effective radius, which can only be considered a rough estimate. Furthermore, observed radiance pairs at visible and solar near infrared wavelengths often do not lie within the range of modeled radiances. In principle, this can be attributed to a lack of small ice particles in the model calculations and to the influence of characteristic vertical structures in the real clouds to the radiance fields.

The objective of this Visiting Scientist Activity (VSA) is to contribute to an improvement of the algorithms for the retrieval of cloud optical thickness and ice water path for ice clouds. There are a number of uncertainties with respect to cirrus cloud radiative transfer modeling that deserve attention, such as: crystal shapes and sizes, vertical cloud structure, crystal orientations, spectral reflection of rough sea surfaces. The present study focuses on particle shapes, sizes and vertical cloud structure, the latter being available from the CloudNET experiment (Zadelhoff van et al., 2004).

The outline of this report is as follows. In chapter 2, the tools and methods are introduced that are used for this study, comprising the radiative transfer models, ice crystal phase functions, the lidar/radar method to retrieve ice water path and the CloudNET measurement campaign (Zadelhoff van et al., 2004). In chapter 3, the sensitivity of cloud radiance as observed from satellite to the vertical distributions of ice crystals is presented. The effects of using different crystal types for the calculation of Look-Up-Tables (LUTs) for 0.6 and 1.6 μm reflectances are illustrated in chapter 4. Chapter 5 presents the results of the preliminarily comparison of retrieved cloud properties with CloudNET radar and lidar ground measurements. Finally, the results are summarized and conclusions are drawn in Chapter 6.

Chapter 2

Tools and methods

2.1 Radiative Transfer Models

Within the CM-SAF, the Doubling Adding KNMI (DAK) radiative transfer model is used to relate cloud properties to simulated cloud reflectances. DAK is developed for line-by-line or monochromatic multiple scattering calculations at UV, visible and near infrared wavelengths in a horizontally homogeneous cloudy atmosphere using the doubling-adding method (e.g. de Haan et al., 1987). The Spherical Harmonic Discrete Ordinate Method SHDOM (Evans, 1998) was developed for modeling radiative transfer in inhomogeneous three-dimensional media. SHDOM uses an iterative procedure to compute the source function of the radiative transfer equation on a grid of points in space. The angular part of the source function is represented by a spherical harmonics expansion mainly because the source function is computed more efficiently in this way than in the commonly used Discrete Ordinate Radiative Transfer method DISORT (Stamnes et al., 1988). A discrete ordinate representation is used in the solution process. The number of iterations increases with increasing single scattering albedo and optical thickness. The present study uses a Monte-Carlo method which allows a more flexible treatment of input scattering and absorption properties than SHDOM, while SHDOM is used for the calculations of radiance-to-cloud properties LUTs.

The Monte Carlo model used here (Macke et al., 1999) is a forward scheme with a local estimate procedure for radiance calculations. It is a straightforward model that can be extended from one-dimensional to two or three-dimensional calculations. Monte Carlo treats multiple scattering as a stochastic process. The phase function governs the proba-

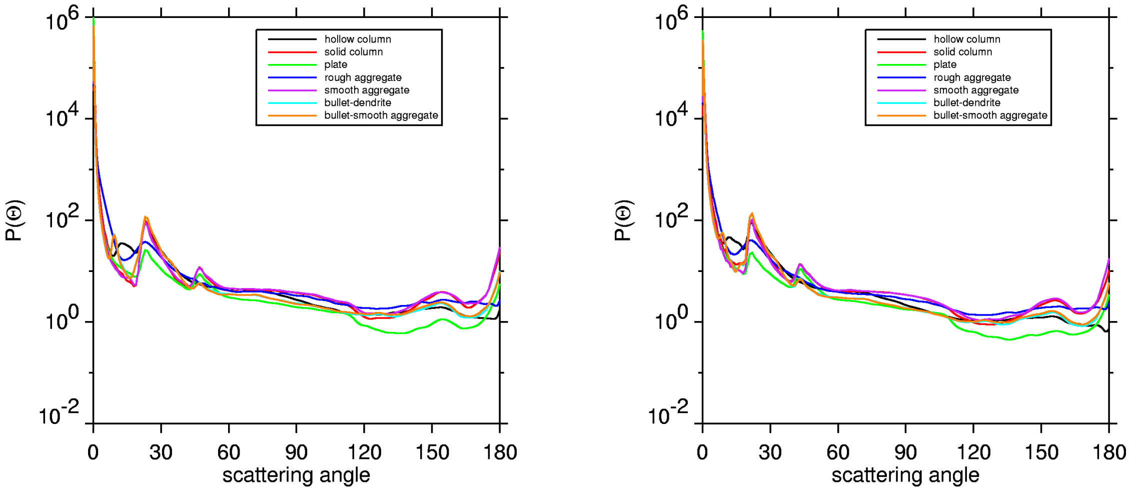

(a) $\lambda = 0.60$ µm

(b) $\lambda = 1.60$ µm

Figure 2.1: *Phase functions from the Ping Yang database for different ice crystal shapes;* $(\Theta_0, \Phi_0) = (0, 0)$*,* $(\Phi) = (0, 180)$*,* r_{eff} *= 25* µm *and two wavelengths*

.

bility of scattering in a specific direction. Photon packages are emitted from a source (e.g. the sun or a lidar device) and undergo scattering and absorption events inside a predefined three-dimensional cloudy atmosphere until the energy of the package falls below a certain threshold, the photons escape from the system, or until they are absorbed by particles or by the surface (forward scheme). At each scattering event, the intensity that contributes to predefined sensor viewing angles is calculated (local estimate procedure), which enables rapid and accurate radiance calculations.

2.2 Phase functions

The phase functions of ice crystals depend on their size, shape, and orientation. Therefore, phase functions in real ice clouds are always an average over an ensemble of ice crystals with varying orientations, shapes and crystal sizes.

The theory, which can be used to calculate phase functions depends on the crystals shape and size. As ice crystals are not spherical like water droplets and have a more complex internal structure, Mie theory (van de Hulst, 1957) cannot be applied. Common alter-

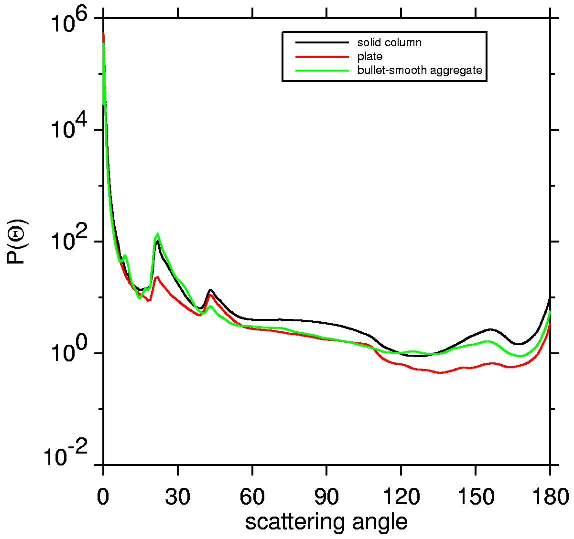

Figure 2.2: *Phase functions from Ping Yang database for columns, plate and bullet ice crystals;* $(\Theta_0, \Phi_0) = (0, 0)$, $(\Phi) = (0, 180)$, r_{eff} *= 25 μm and* λ *= 1.60 μm*

.

natives are the T-Matrix method (Mishchenko et al., 2000) especially used for spheroids and circular cylinders, the Finite Differences Time Domain FDTD (Yang and Liou, 1996a) method for small to moderate size hexagonal cylinders, the Discrete Dipole Approximation DDA (Draine and Flatau, 1994) for arbitrary shaped small particles or the Geometric Optics GO method (Born and Wolf, 1999) for arbitrary shaped large particles.

During the VS-Activity 'Cloud Optical Thickness and Cloud Liquid Water Path Phase 2' (Macke et al., 2003) the cirrus part of the calculated lookup table was based on phase functions from Hess et al. (1998) from GO calculations for imperfect ice crystals. According to the availability of observed ice particle size distributions and to the applicability of the GO approximations these phase functions hold for ice crystal size distributions with effective radii larger than about 25.0 μm.

For clouds with similar cloud optical thicknesses the simulated DAK cloud reflectances, which are used within the CM-SAF, show a gap between 1.6 μm reflectances of large water droplets (effective radius 24 μm) and small ice crystals (effective radius 30 μm). Due to this gap the retrieval of the cloud thermodynamic phase tends to be undecisive for certain pairs of 0.6 and 1.6 μm radiances. One physical explanation for the gap between ice and water cloud lookup tables might be the fact that smaller and more isotropically scattering ice particles are not accounted for in the LUT. The improved geometric optics method GOM2 by Yang and Liou (Yang and Liou, 1996b) in combination with the Finite

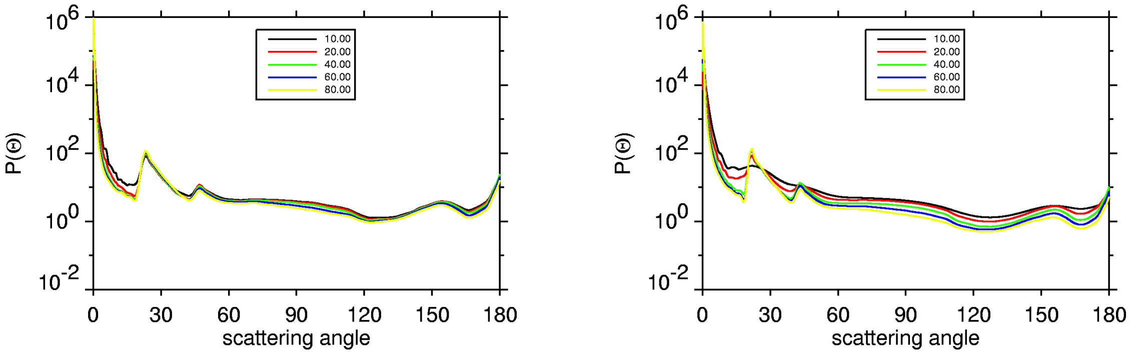

(a) λ = 0.60 µm

(b) λ = 1.60 µm

Figure 2.3: *Phase function for column ice crystals and various effective radii and two wavelengths;* $(\Theta_0, \Phi_0) = (0, 0)$, $(\Phi) = (0, 180)$

.

Difference Time Domain Method FDTD by (Yang and Liou, 1996a) covers essentially the entire range of ice crystal sizes. While the physical processes are treated more accurately than in the GOM , the hybrid GOM2-FDTD method is restricted to rather simple particle geometries. Therefore, the choice between GOM or GOM2-FDTD is a trade-off between accounting for more realistic particle geometries and accounting for a less approximative solution of the scattering problem. Observed fields of reflected (polarized) radiation are better reproduced by GOM phase functions for irregular/distorted ice crystals. However, such crystals must be regarded as some 'equivalent-morphological' models from which real physical quantities like ice water content can not be deduced. The GOM2-FDTD results are related to ice content and other particle properties. Therefore, we decided to use this data set. Another reason in favor of these phase functions are the simple accessibility as it comes with the public available radiative transfer code SHDOM.

Within SHDOM, phase functions for eight different crystal shapes can be extracted. The crystal sizes are distributed following a gamma distribution, which is tuned to observations. The single scattering properties have been produced by Yang et al. (2000). Results are tabulated for 56 wavelength bands in the solar spectrum from 0.2 - 5.0 µm. The 24 different particle sizes vary from 3 to 3500 µm, the 8 ice crystal shapes are solid and hollow columns, plates, dendrites, rough and smooth aggregates and two types of bullets. Figure 2.1(a) shows all eight phase functions as a function of the scattering angle at a non-absorbing wavelength of λ = 0.60 µm and for an effective radius r_{eff} = 25 µm. Due to the different shapes, the different crystals show a slightly different behavior. Especially

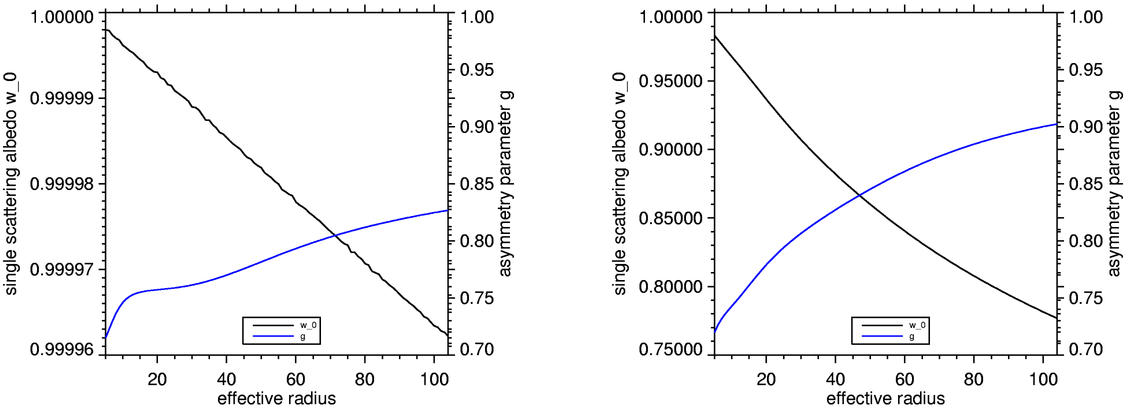

(a) λ = 0.60 µm (b) λ = 1.60 µm

Figure 2.4: *Single scattering albedo and asymmetry parameter as function of effective radius.*

the varying intensities of the halo peaks depend on the different occurrences of 60 and 90 degree ice prisms for the different ice particle geometries.

Similar angular scattering characteristics as discussed above for nearly non-absorbing visible wavelengths are also found at absorbing wavelengths in the solar spectrum. This is because of 1) the small spectral changes in the refractive index of ice and 2) due to the fact that the most dominant angular scattering patterns result from external reflection, direct transmission or ray paths with few internal reflections, which are only slightly attenuated. As an example, Figure 2.1(b) shows the phase functions of hexagonal columns, plates, and bullets at a wavelength of 1.6 µm.

For the present study we narrow our choice to three ice crystal shapes which are considered representative of three typical, but very different crystal types: plates, columns, and bullet-smooth aggregates. The corresponding phase functions are shown in Figure 2.2. The phase function of the plate crystal type (red curve) is the smoothest. Due to the dominance of plane-parallel facets forward scattering is strong and the halos are less pronounced. On the other hand, the phase function of solid columns which consist of several 60° and 90° prisms show strong 22° and a 46° halos. Because of the lack of 90° prisms the bullet-smooth aggregate crystal type misses the 46° halo, but does have a halo at a smaller angle caused by the transmission through pyramidal tops. Again, similar angular scattering behavior is found at λ = 1.60 µm.

Figure 2.3 presents the phase functions for a fixed crystal shape, column ice crystals, for different effective radii (color coded) at the 0.60 and 1.60 μm wavelengths. While the curves at a non-absorbing wavelength of λ = 0.60 μm are very similar, the phase functions at λ = 1.60 μm show a greater spreading and different angular pattern, especially at scattering angles less than 60°, where the halo occurs.

This behavior is easily explained by the increasing absorption with increasing crystal size at absorbing wavelengths. This is more clearly shown in Figure 2.4, where the single scattering albedo and the asymmetry parameter are plotted as a function of effective radius. While the single scattering albedo ω_0 for the visible wavelength stays around 0.99 for nearly all effective radii (Figure 2.4(a)), it changes for the near infrared from ω_0 = 0.78 for r_{eff} = 10 μm up to ω_0 = 0.90 for r_{eff} = 80 μm (Figure 2.4(a)). Note that the use of smallest effective radii of 10 μm compared to the previously used value of 25 μm reduces the smallest possible single scattering albedo from 0.83 to 0.78 and the highest possible asymmetry parameter from 0.00 to 0.74 at 1.6 μm.

2.3 Lidar/Radar Inversion Procedure

In this section a short summary is given of the procedure used to calculate the cloud microphysical properties from combined lidar and radar signals. A detailed description can be found in Donovan and van Lammeren (2001) and Donovan et al. (2001).

The lidar/radar algorithm is based on an inversion procedure where the lidar extinction coefficient (α) is calculated using a Klett-type solution procedure (Klett, 1981) with an appropriate boundary value. As the extinction can be directly related to the single-scattering power at the lidar wavelength, it is important to correctly calculate the fraction of the observed signal due to multiple scattering. The effect of multiple scattering on the lidar return is approximately accounted for by the analytical model of Eloranta (1998). This approach gives good results, compared to full Monte-Carlo calculations, for small lidar opening angles.

In the retrieval the vertical profiles of the lidar derived extinction and radar reflectivity (Z_e) are combined to provide particle sizes. The effective radius R_{eff} is not directly estimated; instead first a lidar/radar effective radius (R'_{eff}) is determined. This R'_{eff} is then used to estimate the true R_{eff}.

The lidar/radar effective radius is defined as

$$(R'_{eff})^4 = \frac{9}{16\pi\rho_{s,f}^2}\frac{\langle M^2(D)\rangle}{\langle A_c(D)\rangle} = R_{eff}\frac{3}{4\pi\rho_{s,f}}\frac{\langle M^2(D)\rangle}{\langle M(D)\rangle} \tag{2.1}$$

where equation 2.1 is used to link the two different effective radii definitions. The brackets denote averaging over the particle size distribution, D the maximum dimension of the particle, M the particle mass, A_c the cross-section area and $\rho_{s,i}$ the density of solid ice. The fraction $\langle M^2(D)\rangle/\langle M(D)\rangle$ depends on the precise particle size distribution and ice crystal habit.

The radar reflectivity, denoted as Z_e, is determined by the squared mass distribution and the extinction by the total cross-sectional area of the particles, R'_{eff} is an invariant function of the ratio between the optical extinction and the radar reflectivity:

$$(R'_{eff})^4 \propto \frac{Z_e}{\alpha} \tag{2.2}$$

where α is the extinction at the lidar wavelength. This relationship is valid for particles that are Rayleigh scatterers at the radar frequency and optical scatterers at the lidar wavelength.

To conclude, R'_{eff} is defined by the observations only. No assumption needs to be made concerning the particle size distribution and ice crystal habit as these are not derived quantities. However, the conversion to the true effective radii (R_{eff}) does depend on assumptions made about the true ice crystal habit and the size distribution characteristics; in particular, the degree of multimodality is important (Donovan, 2003).

2.4 Cloudnet

CloudNET was an EU-funded research project that aimed to use data obtained quasi-continuously at three remote sensing stations for the development and implementation of cloud remote sensing synergy algorithms. The project started on the 1st of April 2001 and ended on the 1st April 2005. The three experimental research sites were situated in Cabauw (The Netherlands), Chilbolton (UK) and Palaiseau (France). Each site was equipped with radar, lidar and a suite of passive instrumentation. The active instruments lidar and cloud radar were used to obtain detailed vertical profiles of important cloud parameters, which cannot be derived from current satellite sensing techniques. A network was operated for a two year period (2003-2004) to build a coordinated, harmonized and joint data archive. The observations have been used to evaluate four operational numerical models and to demonstrate the role that could be played by an operational network of cloud remote sensing stations.

Chapter 3

Sensitivity of reflectances to crystal size distributions

In this section the sensitivity of the solar reflectance to the vertical distribution of crystals with different crystal effective radii is discussed in order to find an explanation for the gap between the LUT for water and ice clouds. Observations of vertical profiles of particle size in cirrus clouds (Zadelhoff van et al., 2004) show a pronounced vertical structure with smallest particles at cloud top, increasing size toward cloud bottom and a slight decrease again near cloud bottom as illustrated in Figure 3.1. This feature is conform our general understanding of ice nuclei forming at the coldest heights, growth along sedimentation until the crystals fall out of the regions of supersaturation where they sublimate to smaller sizes.

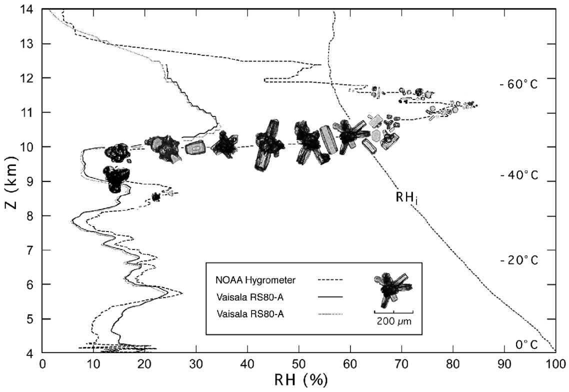

Figure 3.1: *Vertical distribution of relative humidity and ice crystal shape; from Heymsfield and Miloshevich (1995).*

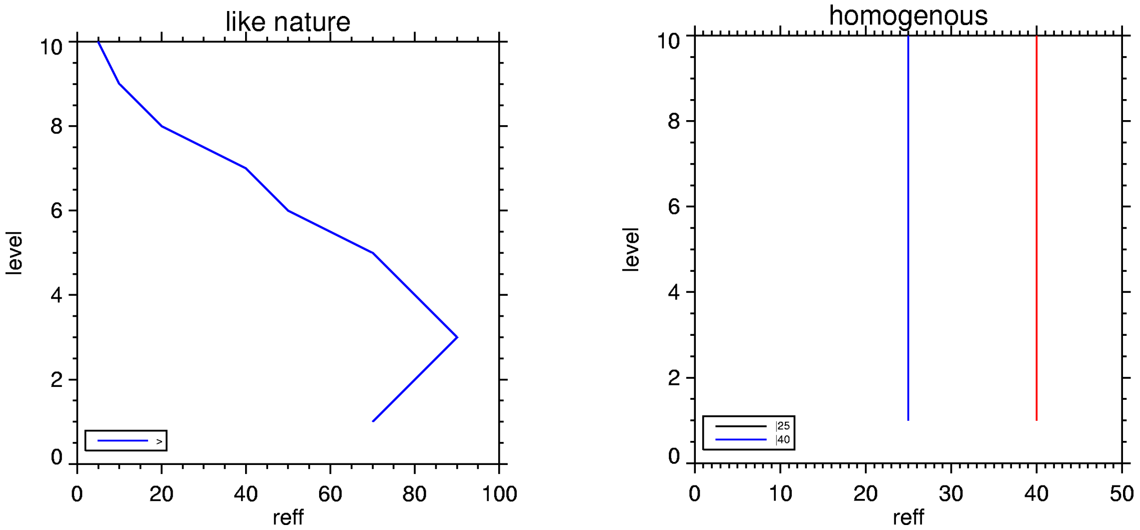

(a) ’like nature’

(b) ’homogeneous 25’(blue), ’homogeneous 40’(red)

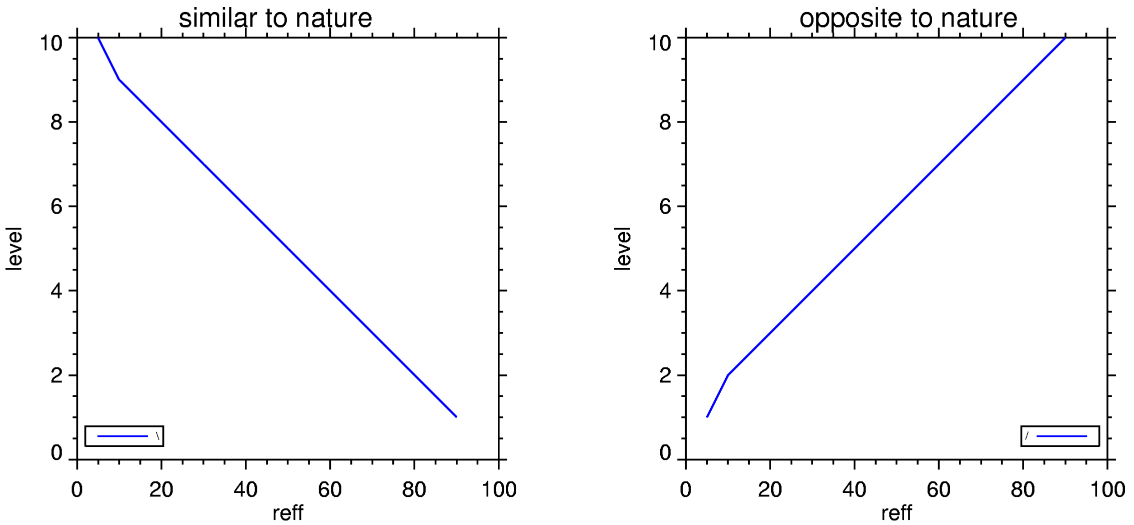

(c) ’similar to nature’

(d) ’opposite to nature’

Figure 3.2: *Vertical profiles of effective radius.*

Furthermore, radiative transfer simulations show that the upper parts of the clouds contribute most to the reflected solar radiation Platnick (2000). Thus, it is to be expected that the choice of ice crystal size and habit near the top of the cirrus clouds considerably influences the intensity and angular pattern of the reflectance functions.

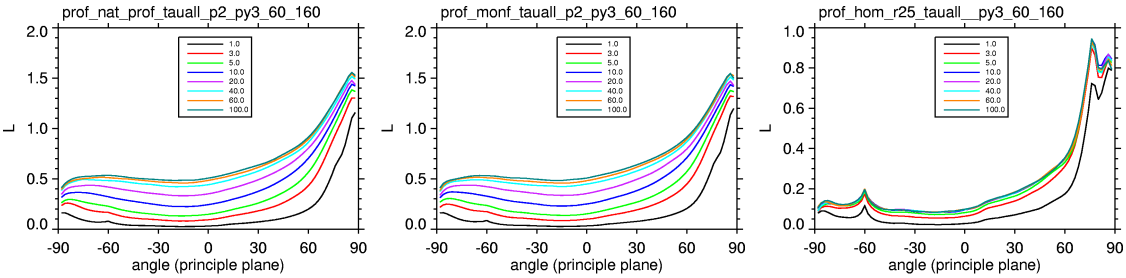

(a) 'like nature' (b) 'similar to nature' (c) 'homogeneous 25'

Figure 3.3: *Reflection function in the principle plane for a fixed ice crystal shape (column) as a function of optical thickness;* $(\Theta_0, \Phi_0) = (60, 0)$, $(\Phi) = (0, 180)$ *at 1.6* μm

.

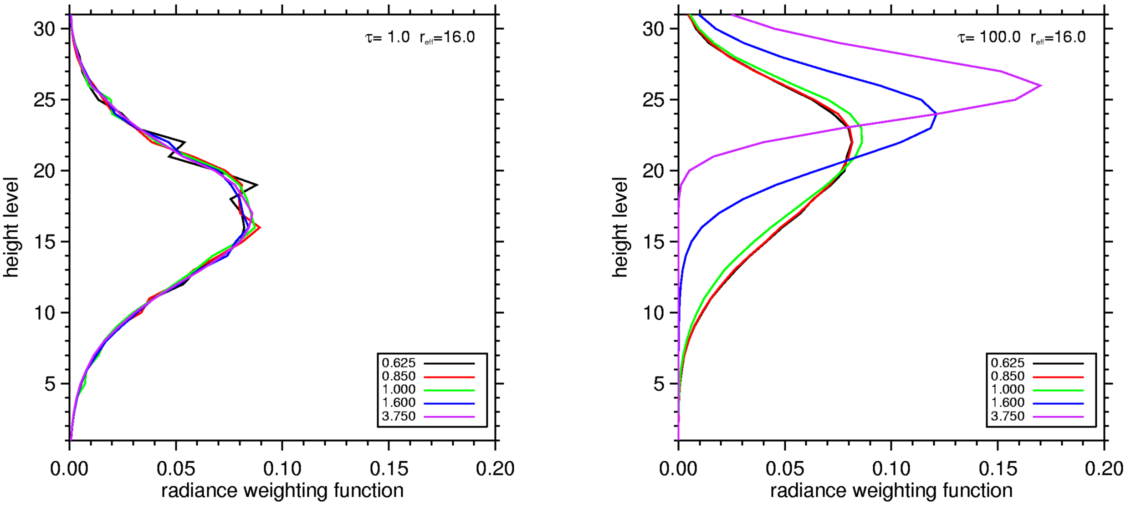

(a) τ=1.0, r_{eff}=16.0 μm (b) τ=100.0, r_{eff}=16.0 μm

Figure 3.4: *Vertical weighting function for a cloud with* τ*=1.0 (left panel) and* τ*=100.0 (right panel) and* r_{eff}*=16.0* μ *for a Gaussian distributed vertical profiles of extinction coefficients. The weighting functions are calculated for the 0.6, 0.8, 1.0, 1.6 and 3.7* μm *wavelengths*

Five different profiles as shown in Figure 3.2 have been selected for this sensitivity study. Figure 3.2(a) resembles the above mentioned typical behavior. Downward into the cloud the effective radius increases from cloud top to the lower cloud levels. From here, the effective radius decreases until the cloud bottom is reached. This profile follows the paper of Zadelhoff van et al. (2004), who investigated cirrus cloud measurements during CloudNET. Additional to this profile, in the following referred to as 'like nature', more

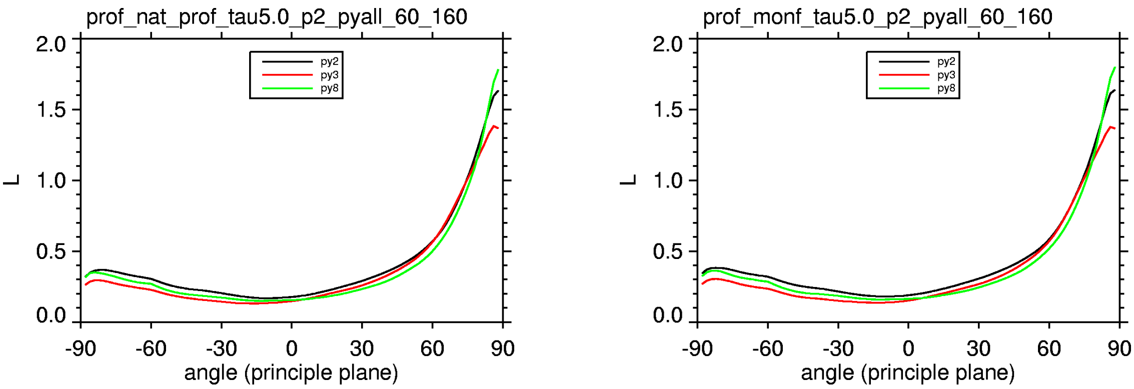

(a) 'like nature'

(b) 'similar to nature'

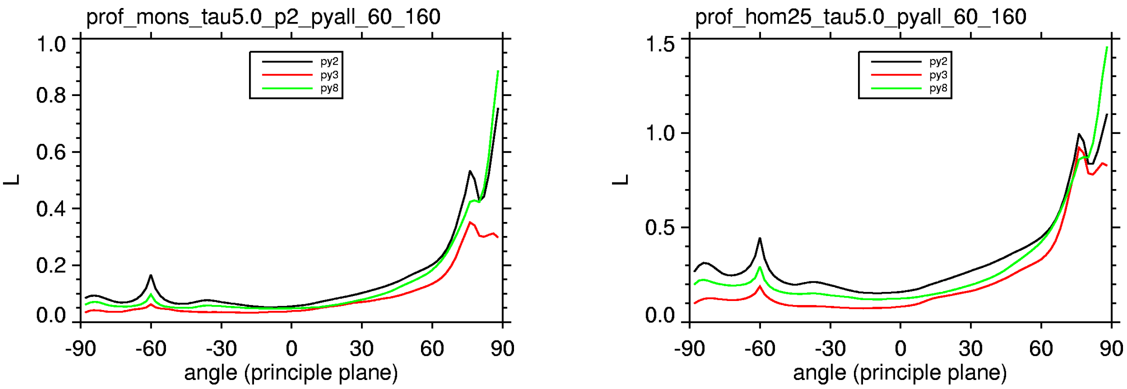

(c) 'opposite to nature'

(d) 'homogenoeus 25'

Figure 3.5: *Reflection function in the principle plane for a fixed optical thickness* ($\tau = 5.0$) *as a function of ice crystal shape;* $(\Theta_0, \Phi_0) = (60, 0)$, $(\Phi) = (0, 180)$

.

theoretical profiles are chosen. Figure 3.2(b) represents two vertically homogeneous profiles for ice crystals with effective radii of 25 μm and 40 μm. These profiles are currently used in the CM-SAF. Two adapted profiles with a homogeneously decreasing effective radius with height ('similar to nature'; 3.2(c)) and its opposite, increasing effective radius with height ('opposite to nature'; 3.2(d)) are used for the intercomparison as well.

To calculate the sensitivity of the reflected solar radiance to these profiles, a number of different situations have been considered.For the radiative transfer calculations, the optical thickness is varied from $\tau = 1.0$ up to $\tau = 100.0$ with a vertically homogeneous distribution of the column extinction coefficient. As mentioned before, all phase functions

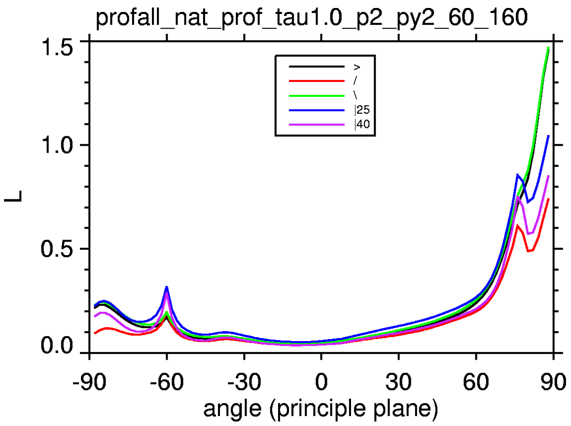

Figure 3.6: *Reflection function in the principle plane for a fixed ice crystal shape (column) and a fixed optical thickness ($\tau = 1.0$) as afunction of the profile;* $(\Theta_0, \Phi_0) = (60, 0)$, $(\Phi) = (0, 180)$

.

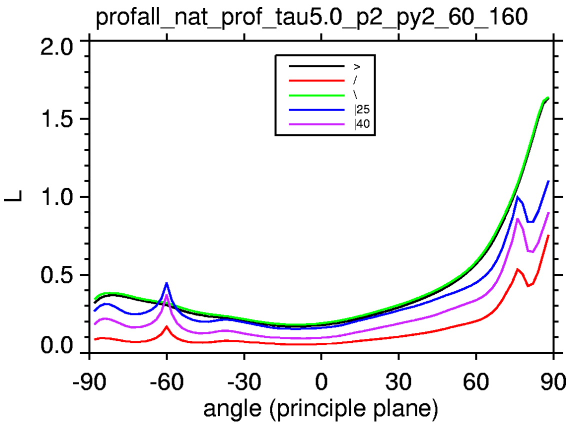

Figure 3.7: *Reflection function in the principle plane for a fixed ice crystal shape (column) and a fixed optical thickness ($\tau = 5.0$) as a function of the profile;* $(\Theta_0, \Phi_0) = (60, 0)$, $(\Phi) = (0, 180)$

.

for column, plate and bullets are taken from Ping Yangs data base. The sun geometry is fixed to a solar zenith angle Θ_0 = 60° and a solar azimuth angle ϕ_0 = 0°. The viewing geometry covers the principle plane ($\phi = 0°, 180°$) with viewing zenith angles from $\Theta = 0°$ to $\Theta = 88°$ with a step width of $\Delta\Theta = 2°$. Results are shown for the near-infrared spectral region (λ = 1.60 μm) since the variance in reflected radiance in the visible spectral band is very small due to the nearly neglectable absorption.

Figures 3.3(a-c) show the changes in the reflection functions due to variations in optical thickness (color coded) for the three profiles 'like nature' 3.3(a), 'similar to nature' 3.3(b)

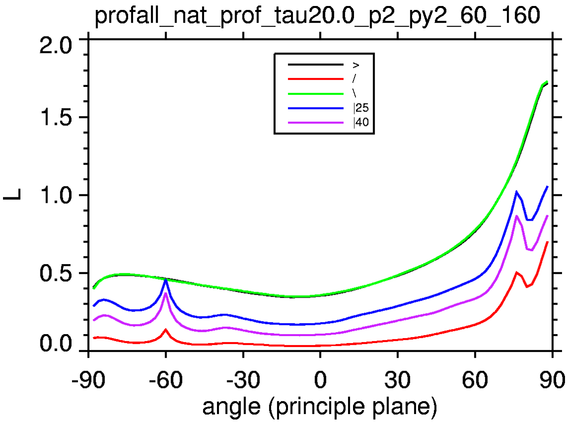

Figure 3.8: *Reflection function in the principle plane for a fixed ice crystal shape (column) and a fixed optical thickness (*$\tau = 20.0$*) as a function of the profile;* $(\Theta_0, \Phi_0) = (60, 0)$, $(\Phi) = (0, 180)$

.

and 'homogenous 25' 3.3(c). A hexagonal ice plate was selected to represent the scattering and absorption properties. The other ice particle habits show essentially the same behaviour.

Not surprisingly, the reflection function is mostly affected by optical thickness. Profile-induced differences are less pronounced. The two profiles with smaller ice crystals in the upper part of the cirrus cloud show considerably larger radiances compared to the homogeneous profile. This is a direct consequence of the more isotropically scattering smaller ice crystals near the cloud tops. For the 'opposite to nature' scenario, the larger ice crystals near the cloud top (compared to the inhomogeneous cases) are scattering the incoming radiation more into the forward direction which leads to an increased transmission resp. reduced reflected radiance. These profile-induced differences are strongest for optically thick cirrus clouds. For thin clouds, only few scattering processes occur[1] and vertical inhomogoneity is not "resolved" by the solar photons.

Although the profiles in Figure 3.3 (a) and (b) show differences in the lower cloud levels, the resulting reflection functions are nearly identical. This leads to the conclusion that the shape of the reflection function is mainly governed by the general shape of the profile and is not influenced by variability in the lowest few cloud levels. Thus, the reduction of ice crystal sizes in the lower (sedimenting) part of cirrus clouds caused by melting pro-

---

[1] The average number of scattering processes equals the optical thickness divided by the cosine of the solar zenith angle.

cesses does hardly effect the radiative properties. Again, for optically thin clouds only few photons are scattering due to the strong transmission. For optically thick clouds, few photons are scattered in this region due to the fact that most scattering processes occur in the upper cloud parts.

In order to assess which cloud regions contribute most to the observed reflectances, spectral weighting functions were calculated (see Figure 3.4 a,b) based on the Local Estimate Technique in Monte-Carlo radiative transfer. In general, the weighting function peaks in the upper parts of the cloud as the radiation enters there. Figure 3.4(a) shows the weighting functions at five different wavelengths for a very thin water cloud with an optical thickness of τ=1.0 and a fixed effective radius r_{eff}=16.0 µm. Because of the small optical thickness, all curves resemble the vertical profile of the extinction coefficient. Most information origins from the part of the cloud where the extinction coefficient is largest. At larger optical thicknesses (τ=100.0, Figure 3.4(b)) the different spectral weighting functions are stronger separated. With increasing absorption, the maximum of the weighting function is moving upward and more information origins from the upper part of the cloud.

To better understand the sensitivity of the reflected radiance on the crystal type, Figures 3.5(a-d) show the reflection function for a cloud with a fixed optical thickness ($\tau = 5.0$) for three different ice crystal shapes: column (black), plate (red) and bullet (green). Again, these calculations have been performed for different vertical profiles.
For all profiles, the radiance is most sensitive to the ice crystal shape. For all viewing zenith angles ice columns show the largest radiance followed by bullets and plates. While the impact of the crystal shape on the radiance pattern is rather small for the profiles 'like nature' (Figure 3.5(a)) and 'similar to nature' (Figure 3.5(b)), it increases for the other two profile types ('opposite to nature' and 'homogeneous 25'. The 'like nature' and 'similar to nature' profiles lead to a very smooth angular scattering characteristic with no pronounced scattering behavior in the forward and backward scattering region. As mentioned above, the smaller and more isotropically scattering ice crystals in the upper parts of the cloud smooth out the more accented (stronger pronounced halo peaks) scattering events that occur at the larger crystals in the lower parts of the clouds. Of course, the situation is reversed for the 'opposite to nature' profile. Furthermore, the larger crystals at the cloud top block the contribution from crystals in the lower cloud parts. Therefore, the pronounced angular scattering characteristics of the larger crystal more strongly affects the angular pattern of the reflection function. For a vertically homogeneous profile the reflection function depends on the ice crystal shape only. It follows that the differences in

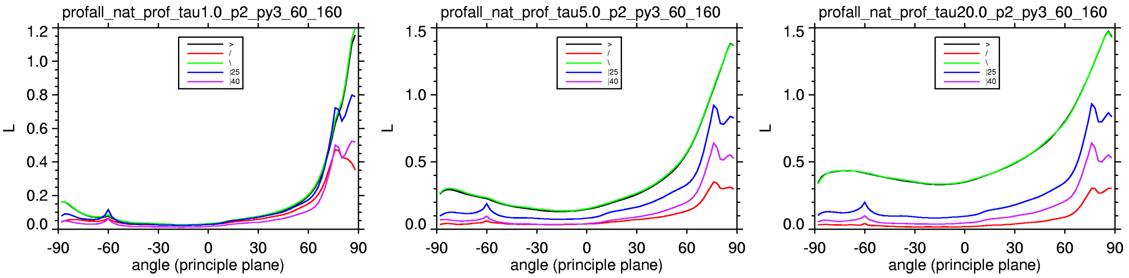

(a) $\tau = 1.0$ (b) $\tau = 5.0$ (c) $\tau = 20.0$

Figure 3.9: *Reflection function in the principle plane for a fixed ice crystal shape (plate) as function of the profile;* $(\Theta_0, \Phi_0) = (60, 0)$, $(\Phi) = (0, 180)$

.

the scattering phase functions directly explain the different angular pattern of the reflection function.

Finally, the remaining diagrams in this chapter show the reflection function for a fixed crystal shape and a fixed optical thickness as a function of the vertical profile ('like nature', black; 'opposite to nature', red; 'similar to nature', green; 'homogeneous 25', blue and 'homogenous 40' purple) only.

Figure 3.6 shows the column crystal based reflection function for a cirrus cloud with optical thickness $\tau = 1.0$. Even for such optically thin clouds some profile induced differences occur. The two reflection functions for the 'like nature' and the 'similar to nature' profile are nearly identical for the chosen optical thickness. The two curves for the homogenous profiles do show, apart from the different intensity of the halo, nearly the same shape but different values. The reflected radiance increases with decreasing effective radius. The graph for the 'opposite to nature' profile does shown a similar behavior compared to the homogeneous profile. Only the values in the forward and the backward direction are slightly smaller.

Figure 3.7 compares profile-dependent differences in the reflection function for an optical thickness $\tau = 5.0$. Again, the two functions for the profiles 'like nature' and 'similar to nature' are nearly identical. As seen from the example with $\tau = 1.0$ the reflection functions are very smooth. Again, all other profiles provide reflection functions with similar shape but different values. In comparison to the optically thinner cloud in Figure 3.6 ($\tau = 1.0$)

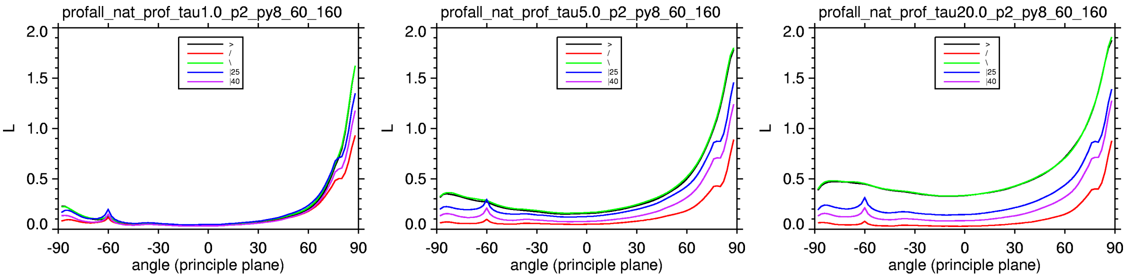

(a) $\tau = 1.0$ (b) $\tau = 5.0$ (c) $\tau = 20.0$

Figure 3.10: *Reflection function in the principle plane for a fixed ice crystal shape (bullet) as a function of the profile;* $(\Theta_0, \Phi_0) = (60, 0)$, $(\Phi) = (0, 180)$

.

the curves are more separated. The profile with the largest crystals at cloud top provides the smallest radianace values for the same reasons as explained above.

In order to get a feeling for the profile-induced radiance variations for optically thick cirrus clouds results for the same settings as before but for an optical thickness $\tau = 20.0$ are shown in Figure 3.8. The reflection function curves are more seperated. This is simply caused by the larger radiance compared to the cases discussed above, which increases the absolute differences between the reflection functions. Furthermore, multiple scattering enhances the influence of the different ice particle scattering properties near cloud top. A scenario with largest microphysical changes near cloud bottom would lead to a smaller spread with increasing optical thickness.

While the previous three figures show results for columnar ice crystals, Figures 3.9 and 3.10 show the reflection functions for plates and for bullets. The general properties of the impact of the varying vertical profile on the reflected radiance are the same, still some differences are worth mentioning. While columns lead to nearly the same curve shape for thin clouds, plates show different radiances, especially for low viewing zenith angles, even for large optical thickness. The reason for this is simply the smaller absolute radiance values compared to the cases for columns and bullets which also reduces the absolut differences due to different profiles of the scattering and absorption properties.

This part of the study has summarized the sensitivity of the solar reflected radiance on variations in the vertical profile of a cirrus cloud. The results emphasize the important role of small ice crystals in the overal reflection behaviour. Especially for thicker cirrus clouds the presence of small crystals near cirrus cloud tops leads to considerably larger values of the reflectance function in the moderately absorbing 1.6 μm wavelength regime.

Chapter 4

LUT Analysis

The results in the previous chapter demonstrate that small ice particles especially at the cloud top lead to a significant brightening of the cloud reflectance. The following section shows examples for new processed cirrus reflectance LUTs with the phase function models by Ping Yang which include smaller ice crystals than in the previous work. A vertical structure of particle sizes has not been used for the LUTs for the lack of generality.

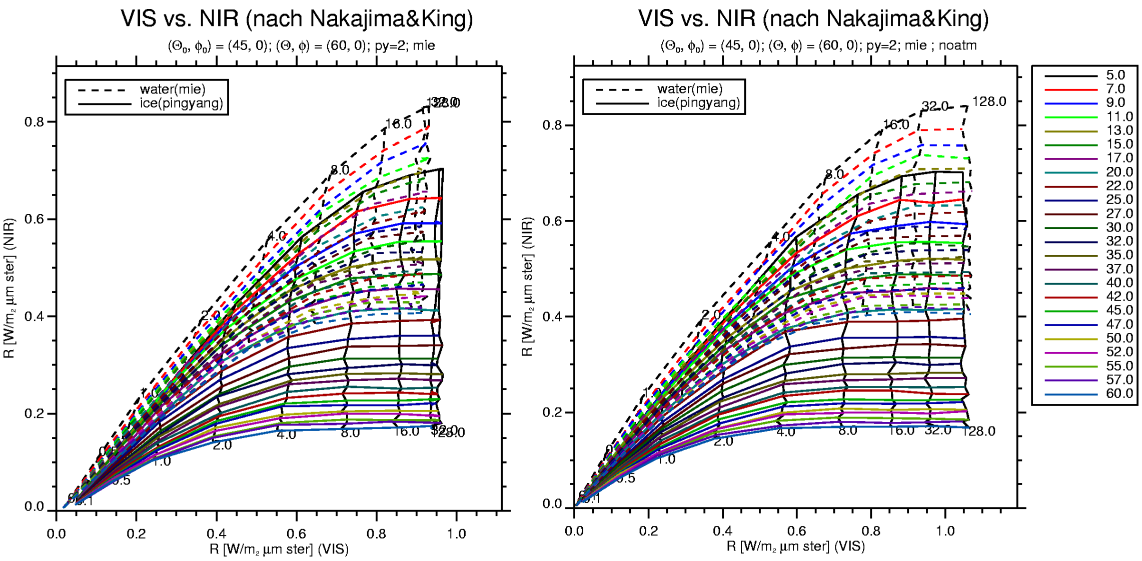
(a) column (with atmosphere)

(b) column (without atmosphere)

Figure 4.1: *Map of radiative transfer simulated reflectances at* $\lambda_{vis} = 0.6\mu m$, $\lambda_{nir} = 1.6\mu m$, *after Nakajima and King (1990), using both a standard atmosphere and no-atmosphere for homogeneous clouds of column crystals and spherical droplets.*

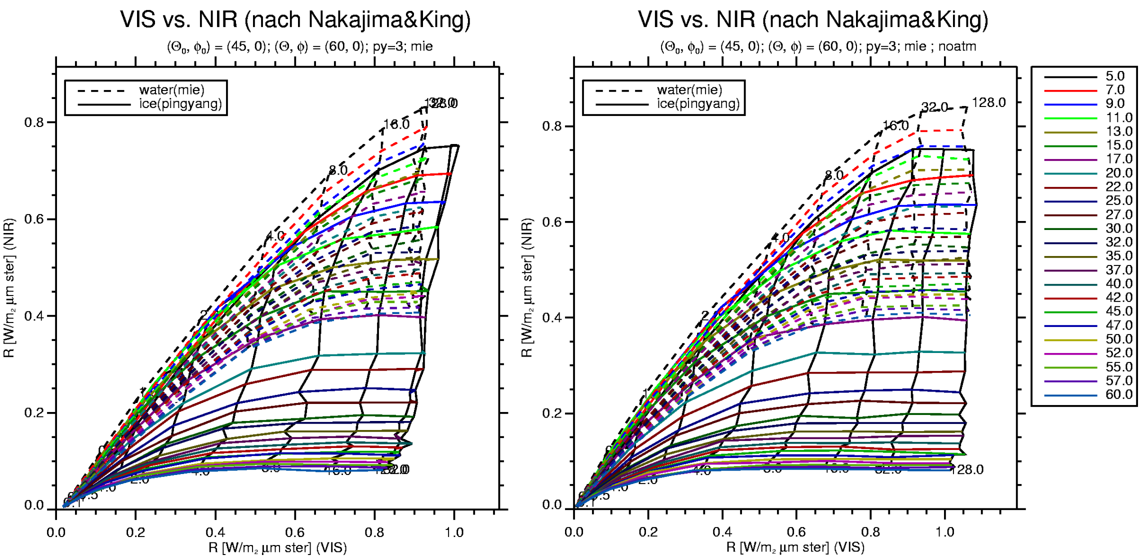

(a) plate (with atmosphere)

(b) plate (without atmosphere)

Figure 4.2: *Similar to Figure 4.1 but than for plate crystals.*

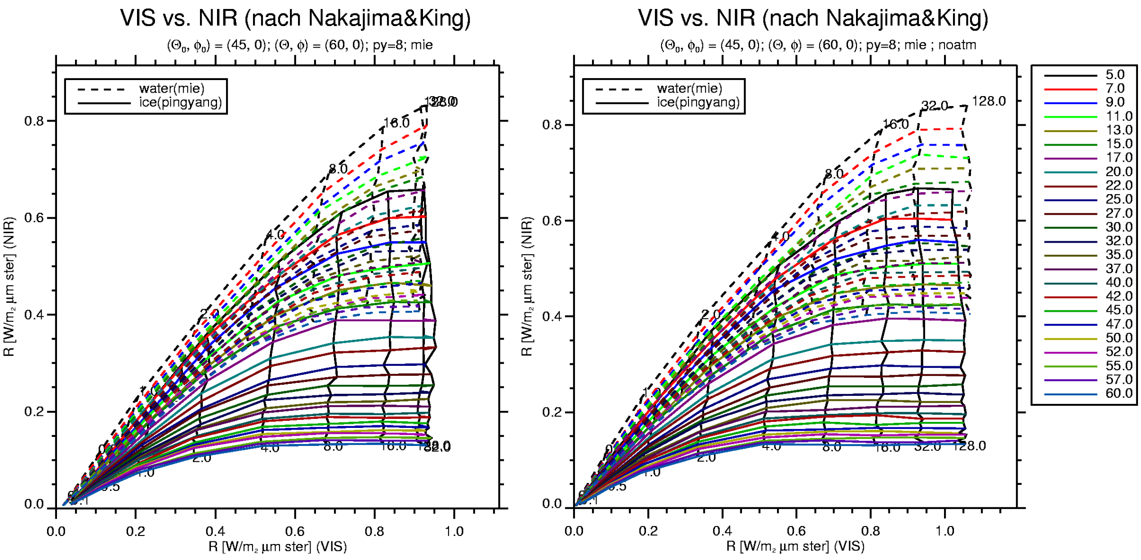

(a) bullet (with atmosphere)

(b) bullet (without atmosphere)

Figure 4.3: *Similar to Figure 4.1 but than for bullet crystals.*

The input clouds for the radiative transfer models consist of one cloud layer with given

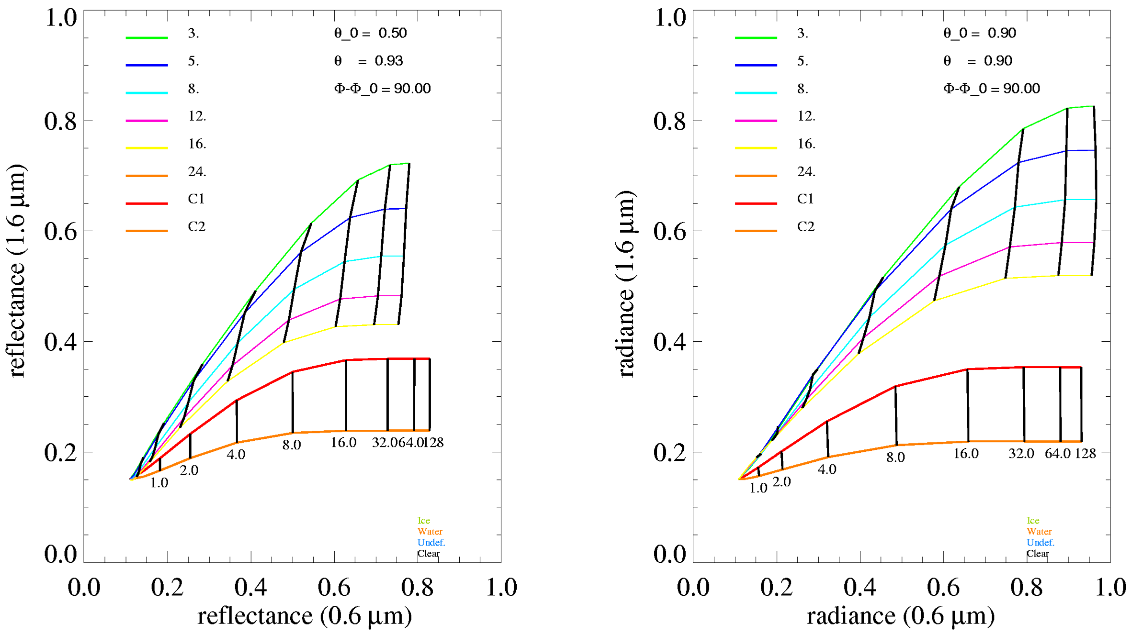

(a) λ = 0.60 μm

(b) λ = 1.60 μm

Figure 4.4: *Reflectance map after Nakajima and King (1990) from the CM-SAF VS-Activity 'Cloud Optical Thickness and Cloud Liquid Water Path Phase 2'.*

optical thickness, effective radius, and ice crystal shape. This layer is surrounded by a standard atmosphere. The LUT has been calculated for solar geometry $(\Theta_0, \phi_0) = (45^\circ, 0^\circ)$ and viewing geometry $(\Theta, \phi) = (60^\circ, 0^\circ)$. The optical thickness has been set to $(\tau = 0.1, 0.5, 1.0, 2.0, 4.0, 8.0, 16.0, 32.0, 128.0)$, the effective radius ranges from r_{eff} = 5.0 μm up to r_{eff} = 60.0 μm. To meet the MSG-Seviri spectral requirements, the wavelengths λ = 0.6 μm for the visible range and λ = 1.6 μm for the near-infrared spectral range have been chosen. The results for ice clouds are based on calculations using the Ping Yang phase functions as distributed within the SHDOM package. To represent water clouds Mie phase functions have been been taken into account.

The results for the three ice crystal shapes are shown in Figures 4.1 for columns, Figures 4.2 for plates and Figures 4.3 for bullets. The simulations have been done both for clouds embedded in a scattering and absorbing gas atmosphere (left panel) and for clouds without surrounding atmosphere (right panel). The calculations related to the water phase functions are displayed as dashed lines, the ice results are indicated by the solid lines. In these plots, the optical thickness is increasing in positive x-axis direction. The reflection in the VIS spectral band is mostly a function of the geometrical cross section, not the length of a particle. The VIS reflection is sensitive to changes in optical thickness of the cloud. In contrast reflection in the NIR band is mostly a function of particle size. Therefore, variations in the effective radius are mainly influencing the NIR reflection. The difference between the calculations that were done with and without atmosphere are nearly identical from which it can be concluded that the similarity between the the LUTs for water and ice clouds are not caused by non-cloud related radiative transfer processes.

For the same effective radius, water clouds show larger NIR radiances than ice clouds. This is mainly due to the larger absorption at the larger particles. Therefore, this behavior can be seen for all three ice crystal habits. Furthermore, the habit-dependent differences in the ice cloud LUTs are small owing to the small influence of shape dependent scattering and absorption differences.

Figure 4.4 presents the LUTs that are currently used in the CM-SAF. In these LUTs there is a relatively large gap between the 1.6 µm reflectances of large spherical droplets (r_{eff} = 24.0 µm) and imperfect hexagonal crystals (r_{eff} = 12.0 µm and r_{eff} = 26.0 µm). The main result of the sensitivity study is that simulated LUTs for water and ice clouds are no longer seperated by a gap in the phase space of reflected non-absorbing and absorbing radiances when ice particles as small as 5 µm effective radius are taken into account. As mentioned in the introduction such a gap is not found in the observations as well and must therefore be regarded as an artefact in the previous model calculations where small ice particles near cloud tops are not accounted for.

Chapter 5

CloudNET

In this chapter the relation of solar reflected radiance as a function of vertically integrated ice water path (IWP) is investigated. The latter has been taken from integrating ice water content (IWC) profiles obtained from the CloudNET campaign described in section 2.4. Figure 5.1 shows an example time series of ice water content profile from this campaign. A closer look into the vertical variability of ice crystal effective radius is given in Figure 5.2. The first section briefly summarizes retrieval methods to derive IWP as well as its microphysical definition, followed by a correlation between observed IWC profiles and calculated radiances at non-absorbing and aborbing wavelengths in the solar spectrum. The main goal is to estimate the uncertainties in this radiance vs IWP correlation (remote sensing algorithms) that is induced by vertical inhomogeneities of the ice cloud properties.

5.1 IWP retrieval methods

CM-SAF

The CM-SAF retrieval of ice water path (IWP) is based on retrieved cloud optical thickness (τ) and effective radius (r_{eff}) from 0.6 and 1.0 μm reflected radiance (Roebeling et al., 2006):

$$\mathrm{IWP} = \frac{2}{3}\tau r_{eff} \tag{5.1}$$

Two fixed effective radii - 30 μm and 40 μm - are used based on C1- and C2 crystal size distributions. Scattering and absorption properties result from the imperfect ice crystal model taken from the COP data library of hexagonal ice crystals (Hess et al., 1998). Knap et al. (2005) demonstrated that these crystals can be used to give adequate simulations of total and polarized reflected radiance of ice clouds.

ISCCP

In ISCCP ice water path is estimated from cloud optical thickness using the following equation (Rossow and Schiffer, 1999):

$$IWP = 0.35\tau r_{eff} \tag{5.2}$$

Where a fixed r_{eff} of 30 μm is used, which corresponds to the settings used in the ISCCP radiative transfer simulations.

Analytic calculation of IWP

The shapes of naturally occurring ice particles in clouds have been found to be highly variable and irregular. Therefore it is not obvious how to express the size of a particle. The size of an ice particle can possibly be expressed as the maximum dimension of the particle, or as the mass equivalent sphere diameter. The mass equivalent sphere diameter Dm means the diameter the particle would have if the particle was an ice sphere with the density of solid ice (=0.91g/cm3), having equal mass m as the particle with a shape that may be different from a sphere, i.e.

$$D_m = \left(\frac{6m}{\rho\pi}\right)^{1/3} \tag{5.3}$$

The maximum dimension of ice particles - defined as the maximum intersection line of two points on the surface of the particle - is in the range from 1 μm to a few mm. The maximum dimension and mass equivalent diameter of a particle can differ significantly from each other. That is, a particle with a maximum dimension of 1000 μm may have a mass equivalent sphere diameter in the order of half of that dimension, depending on the shape of the particle. The particle size distribution psd is here denoted as n(D), where n(D)dD is the concentration of particles with sizes between D and D+dD. If the mass of a particle with dimension D is m(D), then the ice water content (IWC) is

$$IWC = \int_0^\infty m(D)n(D)dD \tag{5.4}$$

For a size distribution of particles, the median mass diameter (D_{median}) and mean mass diameter (D_{mean}) may be suitable size parameters, to represent sizes that contribute significantly to the IWC of the size distribution. The Dmedian is the size of the particles

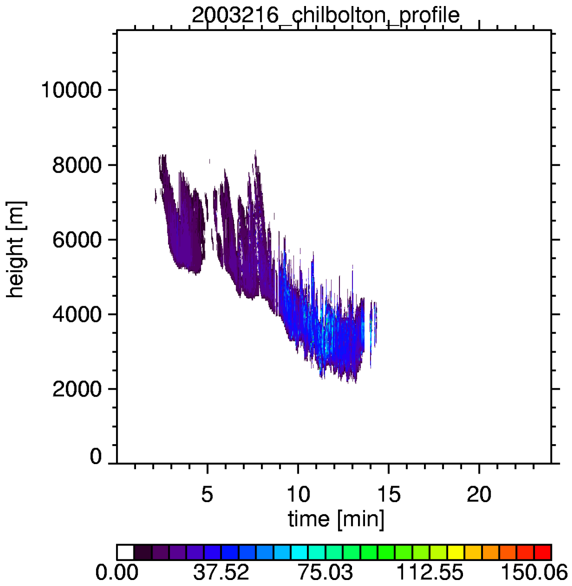

Figure 5.1: *Vertical profile of the effective radius as a function of height and time. Cloudnet, 16 Feburary 2003, Chilbolton*

which divides the IWC into to equal parts, i.e.:

$$\int_0^{D_{median}} m(D)n(D)dD = \frac{IWC}{2} \tag{5.5}$$

The D_{mean} is the size of particles that contribute most to the overall IWC i.e.:

$$D_{mean} = \frac{\int_0^\infty Dm(D)n(D)dD}{\int_0^\infty m(D)n(D)dD} \tag{5.6}$$

$$IWP = \int_{h_{base}}^{h_{top}} IWCdh \tag{5.7}$$

5.2 Analysis of 0.6 and 1.6 µm channel radiance based on observed IWC profiles

The CloudNET project combines ground based lidar and radar measurements to investigate clouds and its temporal variations. The observations used in this study origin from operational measurements in Cabauw, The Netherlands, and Chilbolton, UK. Figure 5.1 shows such a profile that has been retrieved from measurements taken place in Chilbolton at 16 February 2003. This plot shows the variation of effective radius for the time steps 02.00 and 08.00 from observed ice clouds. For each time step, one profile of

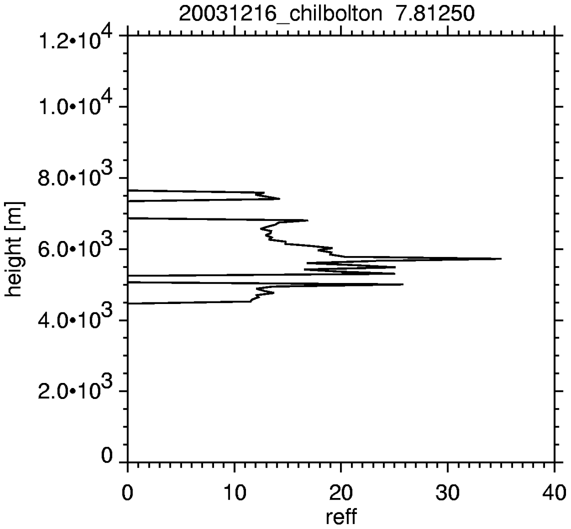

Figure 5.2: *vertical profile of the effective radius as a function of height*

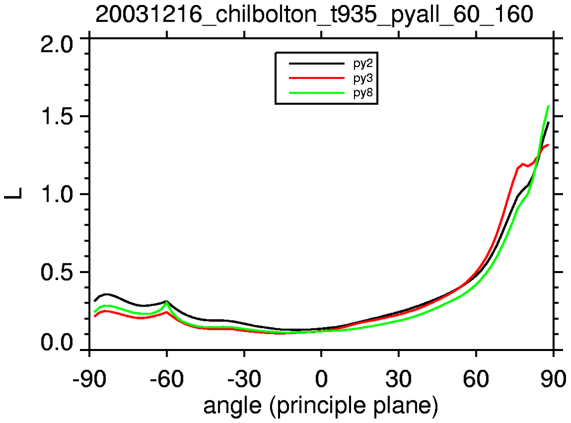

Figure 5.3: *reflection function in the principle plane for a measured profile ; λ = 1.60 μm,* $(\Theta_0, \Phi_0) = (60, 0)$*,* $(\Phi) = (0, 180)$

volume extinction coefficient, effective radius and IWC can be retrieved. Figure 5.2 displays a vertical profile of effective radius. It indicates larger crystals in the lower parts of the cloud and smaller crystals in the upper parts. Figure 5.3 shows the corresponding reflection function for three ice crystal types i.e. for column, plate and bullet. It demonstrates the impact of the different shapes on the reflection.

To obtain a more distinct view of the impact of ice water content profiles on the radiation field, a number of observationally derived vertical profiles have been applied to the Monte-Carlo radiative transfer code to obtain the corresponding reflected solar radiance.

Figure 5.4(a) shows the results of these calculations for the reflected radiances at 0.6 μm wavelength. As commonly used in remote sensing application the IWP values are binned and plotted against the mean radiance corresponding to this IWP bin. The bin width is set to $\Delta IWP = 2.0\ g/m^2$. From this plot the usability of cloud remote sensing can be estimated. The color coding denotes the three different ice crystal shapes column (black), plate (red) and bullet (green). With respect to remote sensing applications, these plots can be separated into three sections. For the first section with IWP $< 20\ g/m^2$ all graphs show a strong sensitivity of reflected radiance on IWP. Cloud IWP can be inferred reliably from observed reflected radiance at 0.6 μm wavelength. The impact of the different ice shapes is very small. However, this behavior changes for clouds with IWP values between 20 g/m^2 and 60 g/m^2. The remote sensing of cirrus clouds in this region depends very much on the assumed shape of the ice crystals. Therefore, a remote sensing retrieval algorithm applicable for this IWP range requires additional information regarding the ice crystal shape, especially in the upper parts of the cloud. Cirrus clouds consisting of hexagonal plates (columns) show the smallest (largest) sensitivity to IWP. A single wavelength remote sensing of IWP may be suitable for clouds consisting of ice columns, and is nearly impossible for cirrus clouds made of ice plates. However, the additional information from the 1.6 μm channel will substantially improve the relation between IWP and observed radiance. For cirrus clouds with IWP beyond 60 g/m^2 the relation between IWP and reflected radiance becomes ambiguous and a single wavelength remote sensing is no longer possible.

Figure 5.4(b) shows the relation between reflected radiance and IWP in the reverse way. Now, the radiance values are binned in radiance bins with $\Delta L = 0.1\ W/m^2$ bin width. On the ordinate the mean IWP corresponding to the radiance bin is plotted. The corresponding variance (squared standard deviation) within each radiance bin is plotted in Figure 5.5. Again the color coding denote the choice of ice crystal shape with columns in black, plates in red and bullets in green. This plot demonstrates the impact of the ice crystal shape on the quality of an IWP retrieval. For small radiance values the impact of the crystal shape is very small. The spread in IWP for the same radiance bin increases for radiances $0.15\ W/m^2 < L < 0.5\ W/m^2$ and decreases again for larger radiance values. The latter is caused by increasing multiple scattering, which smooths out shape dependent scattering differences.

Figures 5.6(a,b) shows the results of the radiative transfer simulations for the same cloud and illumination conditions but now for the absorbing wavelength $\lambda = 1.60\ \mu m$. Due to the enhanced absorption at this wavelength, a clear relation of radiance and IWP is

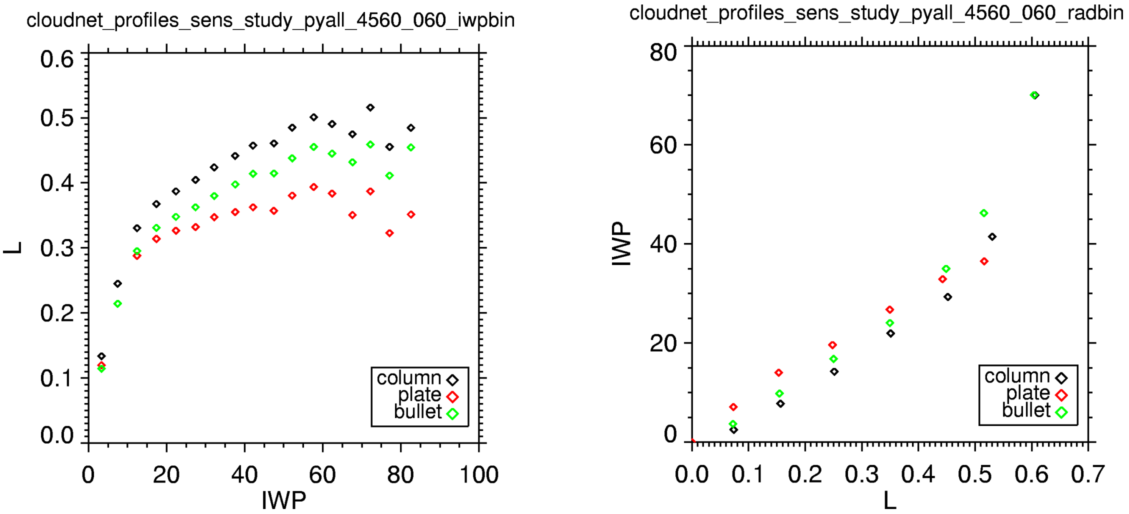

(a) reflected radiance as a function of ice water path

(b) ice water path as a function of reflected radiance

Figure 5.4: *Sensitivity of binned radiance and binned ice water path at λ = 0.6 μm, which were calculated from 3504 CloudNET profiles.* $(\Theta_0, \Phi_0) = (45, 0)$, $(\Theta, \Phi) = (60, 0)$

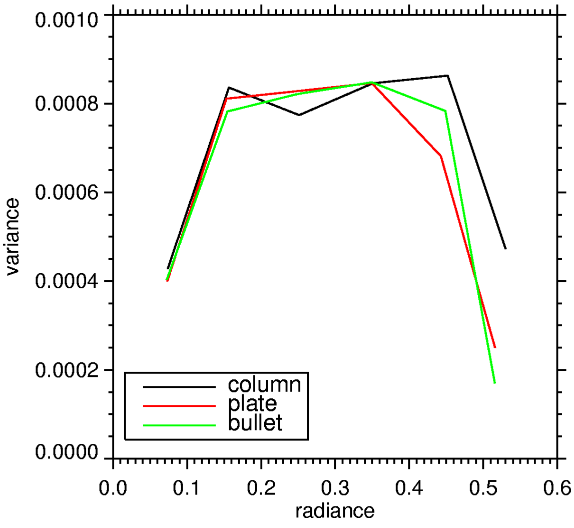

(a) variance in IWP as function of radiance at λ = 0.6 μm

Figure 5.5: *Variance (squared standard deviation) in ice water path for binned reflected radiance for the radiances at λ = 0.6 μm. Average over 3504 CloudNET profiles.* $(\Theta_0, \Phi_0) = (45, 0)$, $(\Theta, \Phi) = (60, 0)$

mainly be found for IWP < 20 g/m^2 (5.6(a)). For IWP values between 20 g/m^2 and 60 g/m^2 the curves show no significant variation in radiances. Also the decrease of reflection with increasing IWP is enhanced as the absorption supports the blocking situation. This can also be seen in Figure 5.6(b). The spread in IWP within one radiance bin is enhanced. While the 0.6 μm channel is mostly sensitive to the cloud optical thickness, the 1.6 μm channel is mostly sensitive to the effective radius. The interesting feature from comparing figures 5.4 and 5.6 is the large difference between the different curves representing different ice crystal shapes. This indicates the importance of choosing the correct crystal type when retrieving the IWP of observed clouds. For IWP values larger than 60 g/m^2 there is a weak relationship of decreasing radiances as the IWP increases. This phenomenon may indicate conditions where the 1.6 μm refletances are mainly a function of absorption, and optical thickness variations do not effect the radiance anymore. For these conditions clouds with larger ice crystals will appear darker than clouds with small ice crystals.

Figure 5.7 presents the variance (squared standard deviation) within each radiance bin for column, plate and bullet crystals for the 1.6 μm wavelength. This plot demonstrates the impact of the ice crystal shape on the quality of an IWP retrieval. For small radiance values the impact of the crystal shape is very small. The spread in IWP for the same radiance bin increases for radiances 0.2 W/m^2 < L < 0.3 W/m^2 and decreases strongly for larger radiance values. Note that the low variances at radiances below 0.2 W/m^2 result from the higher correlation between radiance and IWP that are observed for both thin clouds (IWP < 20 g/m^2) and thick clouds (IWP > 60 g/m^2). The strong decrease in variance for radiances larger than 0.3 W/m^2 is not significant, because there are very few cases with such high radiances.

The cloud-radiance correlations described in this chapter are rather weak for IWP > 20 g/m^2 at $\lambda = 0.6$ μm and for 20 g/m^2 < IWP < 60 g/m^2 at $\lambda = 1.60$ μm wavelengths, which is caused by the variability in ice water content and particle shapes. The analysis of the 1.6 μm reflected radiances reveals for IWP > 60 g/m^2 an increased correlation with the reflected radiances, which suggests the influence of effective particle size variations on the IWP retrievals. A combined use of both wavelengths certainly will improve the correlation and will also provide estimates of effective particle size. To this end, a larger set of observed IWC profiles is required to cover most occurring cirrus cloud realizations, i.e. to provide look-up-tables that can be applied to observed reflected radiances.

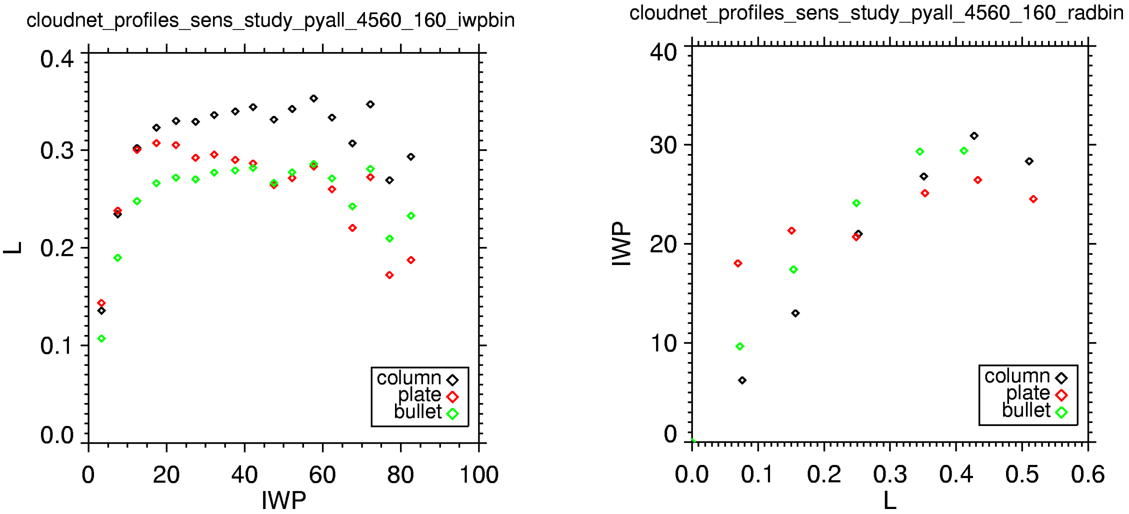

(a) reflected radiance as a function of ice water path

(b) ice water path as a function of reflected radiance

Figure 5.6: *Sensitivity of binned radiance and binned ice water path at λ = 1.6 µm, which were calculated from 3504 CloudNET profiles.* $(\Theta_0, \Phi_0) = (45, 0)$, $(\Theta, \Phi) = (60, 0)$

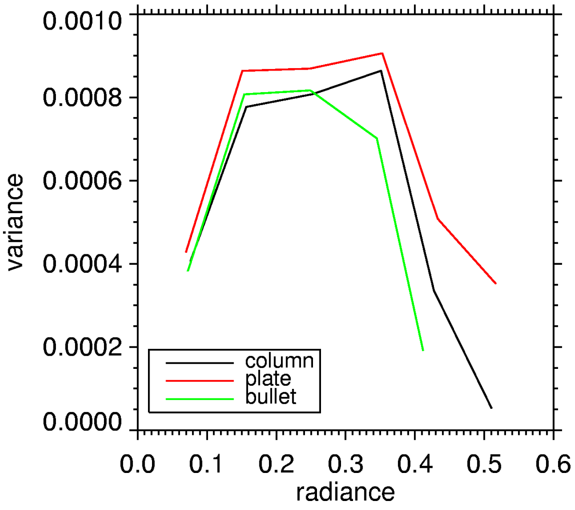

(a) variance in IWP as function of radiance at λ = 1.6 µm

Figure 5.7: *Variance (squared standard deviation) in ice water path for binned reflected radiance for the radiances at λ = 1.6 µm. Average over 3504 CloudNET profiles.* $(\Theta_0, \Phi_0) = (45, 0)$, $(\Theta, \Phi) = (60, 0)$

Chapter 6

Conclusions

The present study has demonstrated that the reflected radiance of ice clouds distinctly depends on the vertical profile of particle size. Furthermore, more realistic profiles with smaller particles near the cloud top lead to a significant brightening of the cloud which moves the modeled spectral reflected radiance closer to the observations. The fact that modeled reflected radiances are quite similar for observed and "nature like" profiles of particle size and that both differ from the previously used vertically homogeneous clouds strongly suggests that some "general" vertical profile would improve the remote sensing retrievals. However, since such profiles do not exist, we propose to make intensive use of experimentally derived profiles from combined ground based lidar/radar measurements performed at KNMI and elsewhere. This attempt enables to 1) use an unbiased profile (on average), and 2) to estimate the retrieval error due to the natural variability vertical profiles of extinction and particle size. Future research will investigate to what extend the variability in cirrus cloud vertical profiles can be narrowed down by means of classification into cloud classes that can be identified from the satellite measurements. Specifically for the temporarily high resolved SEVIRI measurements the age of the cirrus clouds may be a promising parameter, since young cirrus have distinctly different microphysical properties than aged cirrus clouds.

Single scattering and absorption properties of ice particles have been taken from a combination of exact scattering methods (FDTD, improved geometric optics, classical geometric optics) that cover the entire range of particle sizes. We propose that this approach is superior to the use of geometric optics phase functions which allow no physically based link between reflected radiances and ice water path. However, the combined approach does not allow for surface and internal irregularities which are often observed in cirrus clouds. Therefore, a combination of ice water path retrievals from both methods together with ground based IWP from radar/lidar measurements is required to estimate the accuracy of both methods.

The comparison of IWP from combined lidar/radar observations and co-located MSG-retrievals is rendered difficult due to different temporal and spatial sampling of both methods. Still, it provides a direct validation of the satellite retrieval.

Finally, we note that the present sensitivity study can not be very conclusive in terms of quantifying cirrus cloud retrieval errors. All possible one-dimensional cloud versus radiance sensitivities have been calculated, presented and briefly discussed for one specific viewing and illumination geometry. The results show that the correlation between visible reflected radiances (λ = 0.6 μm) and IWP decreases for IWP values larger 20 g/m^2, while the correlation vanishes for IWP larger than 60 g/m^2. However, the correlation between near infra-red reflected radiances (λ = 1.6 μm) and IWP is most significant for IWP values smaller than 20 g/m^2 or larger than 60 g/m^2. It is suggested that the increased correlation for IWP values larger than 60 g/m^2 results from particle size variations. Above presented findings suggest that IWP retrievals may be improved by using a multi-dimensional approach, which combines the differences in retrieved and true optical thickness and ice crystal effective radius as a function of vertical cloud structure of ice water content and ice crystal size. However, such an approach requires LUTs of the reflected radiances at both wavelengths and their variability which in turn can only be constructed from a tremendously large number of radiative transfer calculations. As the required input information is available from CloudNet and other measurment campaigns it appears promising to tackle this rather computational problem at a later stage.

Bibliography

Born, M. and E. Wolf, 1999: *Principles of Optics*. Cambridge University Press, Cambridge.

de Haan, J. F., P. B. Bosma, and J. W. Hovenier, 1987: The adding method for multiple scattering calculations of polarized light. *Astronomy and Astrophysics*, **183**, 371–391.

Donovan, D., 2003: Ice-cloud effective particle size parameterization based on combined lidar, radar reflectivity, and mean doppler velocity measurements. *J. Geophys. Res.*, **108**.

Donovan, D. and A. van Lammeren, 2001: Cloud effective particle size water content profile retrievals using combined lidar and radar observations. PartI: Theory and simulations. *J. Geophys. Res.*, **106**, 27425–27448.

Donovan, D., A. van Lammeren, and R. Hogan, 2001: Cloud effective particle size water content profile retrievals using combined lidar and radar observations. PartII: Comparison with IR radiometer and in-situ measurements of ice clouds . *J. Geophys. Res.*, **106**, 27449–27464.

Draine, B. and P. Flatau, 1994: Discrete-dipole approximation for scattering calculations. *J. Opt. Soc. Am.*, **11**, 1491–1499.

Eloranta, E., 1998: Practical model for the calculation of multiply scattered lidar returns. *Appl. Opt.*, **37**, 2464–2472.

Evans, K., 1998: The Spherical Harmonics Discrete Ordinate Method for three-dimensional atmospheric radiative transfer. *J. Atmos. Sci.*, **55**, 429–446.

Hess, M., R. Koelemeijer, and P. Stammes, 1998: Scattering matrices of imperfect hexagonal ice crystals. *J. Quant. Spectrosc. Radiat. Transfer*, **60**, 301–308.

Heymsfield, A. J. and L. M. Miloshevich, 1995: Relative humidity and temperature influences on cirrus formation and evolution: Observations from wave clouds and FIRE II. *Journal of the Aeronautical Sciences*, **52**, 4302–4326.

Klett, J., 1981: Stable analytical inversion solution for processing lidar returns. *Appl. Opt.*, **20**, 211–220.

Knap, W., L. Labonnote, G. Brogniez, and P. Stammes, 2005: Modeling total and polarized reflectances of ice clouds: evaluation by means of POLDER and ATSR-2 measurements. *Appl. Opt.*, **44**, 4060–4073.

Macke, A., S. Meyer, and R. Roebeling, 2003: Cloud optical thickness and cloud liquid water path phase 2. scientific report, CM-SAF.

Macke, A., D. Mitchell, and L. von Bremen, 1999: Monte Carlo radiative transfer calculations for inhomogeneous mixed phase clouds. *Phys. Chem. Earth (B)*, **24**(3), 237–241.

Mishchenko, M., L. Travis, and A. Macke, 2000: *Light Scattering by Nonspherical Particles*, chapter T-Matrix Method and Its Applications, pp. 147–173. Academic Press., New York.

Nakajima, T. and M. D. King, 1990: Determination of the optical thickness and effective particle radius of clouds from reflected solar radiation measurements. Part I: Theory. *J. Atmos. Sci.*, **47**, 1878–1893.

Platnick, S., 2000: Approximations for horizontal photon transport in cloud remote sensing problems. *J. Quant. Spectrosc. Radiat. Transfer*, **68**, 75–99.

Roebeling, R., A. Feijt, and P. Stammes, 2006: Cloud property retrievals for climate monitoring: implications of differences between SEVIRI on METEOSAT-8 and AVHRR on NOAA-17. *J. Geophys. Res.*,**111**, D20210, doi:10.1029/2005JD006990..

Rossow, W. and R. Schiffer, 1999: Advances in understanding clouds from ISCCP. *Bulletin of the American Meteorological Society*, pp. 2261–2287.

Stamnes, K., S. Tsay, W. Wiscombe, and K. Jayaweera, 1988: Scattering of solar radiation by hexagonal icescattering of solar radiation by hexagonal ice crystals crystals. *Applied Optics*, **27**, 2502–2509.

van de Hulst, C., 1957: *Light Scattering by Small Particles*. Wiley, New York.

Yang, P. and K. Liou, 1996a: Finite-difference time domain method for light scattering by small ice crystals in three-dimensional space. *J. Opt. Soc. Am.*, **13**, 2072–2085.

Yang, P. and K. Liou, 1996b: Geometric-optics-integral-equation method for light scattering by nonspherical ice crystals. *Appl. Opt.*, **35**, 6568–6584.

Yang, P., K. Liou, K. Wyser, and D. Mitchell, 2000: Parameterization of the scattering and absorption properties of individual ice crystals. *J. Geophys. Res.*, **105**, 4699–4718.

Zadelhoff van, G.-J., D. Donovan, H. Baltink, and R. Boers, 2004: Comparing ice cloud microphysical properties using CloudNET and atmospheric radiation measruements program data. *J. Geophys. Res.*, **109**, D24214.